energies

MDPI

Article

Spherical Sb Core/Nb_2O_5-C Double-Shell Structured Composite as an Anode Material for Li Secondary Batteries

Hyungeun Seo, Kyungbae Kim and Jae-Hun Kim *

School of Materials Science and Engineering, Kookmin University, Seoul 02707, Korea; 20131101@kookmin.ac.kr (H.S.); kyungbaekim@kookmin.ac.kr (K.K.)

* Correspondence: jaehunkim@kookmin.ac.kr

Received: 30 March 2020; Accepted: 15 April 2020; Published: 17 April 2020

Abstract: Antimony (Sb)-based materials are considered to be attractive for use in Li secondary battery anodes because of their high capacity. However, their huge volume change during Li insertion-extraction cycling limits their cycle performance. The Sb-active material can be combined with intercalation-based active materials to address these issues. In this study, spherical Sb core/Nb_2O_5 shell structured composite materials were synthesized through a simple solvothermal process and a carbon coating was simultaneously added during heat treatment using a naphthalene precursor. The resulting double-shelled materials were characterized with X-ray diffraction, Raman spectroscopy, X-ray photoelectron spectroscopy, and electron microscopy. The electrochemical test results showed that a reversible capacity of more than 450 mAh g^{-1} was retained after 100 cycles. This improved performance is ascribed to the double-shelled structure. The large volume change of the nano-sized Sb core material was alleviated by the double-shelled structure, which consisted of crystalline orthorhombic Nb_2O_5 and amorphous carbon. The shell materials also aided rapid charge transport.

Keywords: antimony; niobium oxide; composite; anode; Li battery

1. Introduction

With the increasing interest in global warming and the depletion of fossil fuels, research in renewable energy sources such as solar, wind, and bioenergy has been actively pursued. Efficient and reliable energy storage devices are essential to the realization of the full potential of these sources. For instance, Li-ion batteries (LIBs) are the main power source for electric and hybrid vehicles. To meet current market demands, LIBs need to have high energy/power density, low cost, and environmental friendliness. However, commercial LIBs, which commonly incorporate a graphite anode and a lithium transition metal oxide cathode, have limited energy density and power performance [1–3]. Although graphite anodes have reasonable cyclability and low cost, their low theoretical capacity of 372 mAh g^{-1} for LiC_6 after full lithiation limits the energy density of LIBs [4]. To resolve these drawbacks, high-capacity electrode materials have attracted research. Li-alloy-based anode materials are of great interest as a replacement for commercial carbonaceous anodes because of their high theoretical capacity (500–3600 mAh g^{-1}) [5–7].

Sb-based anodes have been considered among the Li-alloy-based materials; they exhibit a high theoretical capacity of 660 mAh g^{-1} for the Li_3Sb phase after full lithiation. As with other Li-alloy based materials, Sb has large volume changes during Li insertion and extraction cycling, causing deterioration of their cycling stability [5]. There have been various efforts to alleviate the volume changes. Several strategies have been found to be effective, such as incorporating carbon, metals, and oxides in composite materials [8–17]. Materials that are inactive to Li have been widely

employed for composites. Intercalation-based materials for Li such as graphite and TiO_2 have been demonstrated to be useful. Although these materials can be active for Li storage, they can also buffer the volume changes of the Li-alloy based materials because their volume changes are very small [18–23]. Recently, niobium pentoxide (Nb_2O_5) materials have attracted much attention for high-rate electrodes in hybrid supercapacitors [24–29]. Nb_2O_5 has pseudo-hexagonal, orthorhombic, tetragonal and monoclinic crystalline polymorphs as a function of their heat treatment temperature [30–33]. One of these crystal structures, orthorhombic Nb_2O_5, exhibited advanced electrochemical properties for Li storage with a moderate capacity of about 200 mAh g^{-1}, fast Li storage, and good cycling stability [25–28]; the material has been incorporated into Li-alloy based composites [34–36].

In this work, we incorporated orthorhombic Nb_2O_5 into an Sb-based composite to improve its electrochemical performance for fast and reversible Li storage. First, a spherical Sb core/Nb_2O_5 shell structured composite was prepared by a solvothermal method. The micron-sized particles consisted of embedded Sb nanoparticles and surrounding niobium oxide shells. Then, the material was heat treated to crystallize the niobium oxide. Carbon coating was simultaneously performed using a naphthalene precursor. The result was an Sb nanoparticle core embedded composite with Nb_2O_5-C double shells. This Sb-core double-shelled composite electrode exhibited better electrochemical properties than a control electrode consisting of mixed material. This result can be attributed to the double-shelled material structure. The material characteristics were examined using several different analytical tools.

2. Experimental Section

Material preparation: A spherical Sb core/Nb_2O_5-C double-shelled composite was prepared via solvothermal and heat treatment procedures. Antimony chloride (2.22 g, $SbCl_3$, Sigma-Aldrich, USA), ammonium niobate oxalate hydrate (1.30 g, $C_4H_4NNbO_9{\cdot}xH_2O$, Sigma-Aldrich, Germany), and Pluronic F-127 (0.80 g, Sigma-Aldrich, Germany) were introduced into a dimethylformamide and ethanol (120 mL, 7:3 volume ratio) solution. This solution was mixed under ultrasonication for 30 min. Then, hydrochloric acid (7 mL, 2 M, HCl, Daejung, Korea) and polyvinylpyrrolidone (0.80 g, PVP, Sigma-Aldrich, China) were added and the mixed solution was stirred for 20 min. After stirring, the solution was transferred into a Teflon-lined steel autoclave (200 mL capacity) and solvothermal synthesis was carried out for 24 h at 200 °C. The resulting product was centrifuged several times while using de-ionized water and ethanol to obtain precipitates, which were then dried at 60 °C. Heat treatment was performed with naphthalene (0.60 g, Sigma-Aldrich, USA) within a vertical furnace in an Ar atmosphere at 600 °C for 2 h. After the treatment, the furnace was automatically cooled down to room temperature.

Material characterization: X-ray diffraction (XRD) was performed using an Ultima IV instrument (Rigaku, Japan) to examine the composite's crystal structure. The chemical states of the composite were examined with Raman spectroscopy (Renishaw) and X-ray photoelectron spectroscopy (XPS, Thermo Scientific Kα). A field-emission scanning electron microscope (JEOL JSM-7401) was employed to characterize the morphology and surface structure of samples. A high-resolution transmission electron microscope (HR-TEM, JEOL ARM-200F) was used with energy-dispersive spectroscopy (EDS) for characterization of the crystal structure and elemental analysis. Thermogravimetric analysis (TGA, TA Instruments Q600) was carried out to determine the carbon content of the composite.

Electrochemical measurement: For working electrode preparation, the active material (70%), a conducting agent (Super P, 15%), and a binder (polyacrylic acid, 15%) were dispersed in a de-ionized water solution. Copper foil was selected as the electrode current collector, and the slurry was coated on the foil. Then, the electrodes were pressed using a roll-presser and dried under vacuum at 80 °C for 12 h. Coin-type half-cells (CR2032 type) were assembled in an argon-filled glove box using the working electrode (12 mm diameter discs), a porous polyethylene separator, and a Li-metal foil counter/reference electrode. The electrolyte was 1 M $LiPF_6$ in ethylene carbonate/diethyl carbonate (3:7 volume ratio) containing 10% fluoroethylene carbonate. Galvanostatic cycling using the coin-type cells was performed in a potential range of 0.001–3.0 V (vs. Li^+/Li) at a specific current of 100 mA g^{-1}.

Discharge and charge correspond to Li insertion and extraction into the working electrode, respectively. For the rate performance test, the specific current was varied from 0.15 to 3.0C (1C = 660 mA g^{-1}) and both discharge and charge were measured at the same rate. For accurate measurement, 20 pre-cycles were carried out at a specific current of 100 mA g^{-1}. Cyclic voltammetry (CV) was carried out at a scan rate of 0.5 mV s^{-1} using a potentiostat/galvanostat (BioLogic VSP).

3. Results and Discussion

Figure 1 shows a schematic of the Sb nanoparticle-embedded composite synthesis with Nb_2O_5-C double shells. During the solvothermal process, the Sb nanoparticles were created from the $SbCl_3$ precursor and amorphous niobium oxide was precipitated surrounding the Sb particles. Consequently, spherical composite particles at micron sizes were produced. The ensuing heat treatment led to the crystallization of the niobium oxide and also to carbon coating on the composite particle from the naphthalene precursor.

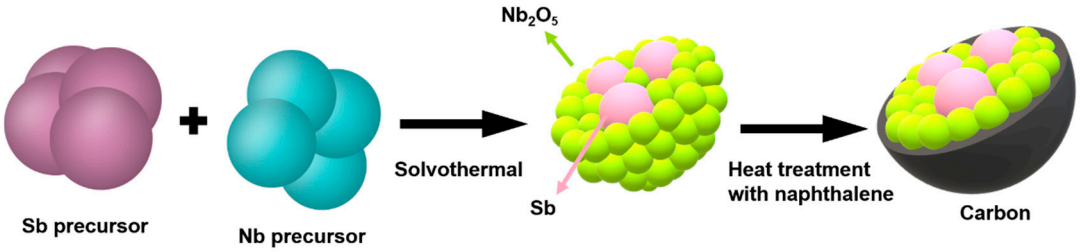

Figure 1. Schematic illustration of the synthesis of the spherical Sb core/Nb_2O_5-C double-shell.

Figure 2 presents the XRD patterns of the as-prepared and heat-treated samples at each step of the synthetic procedure. Diffraction peaks for Sb metal can be seen (ICDD-JCPDS No. 35-0732, rhombohedral) in the as-prepared sample after solvothermal synthesis. However, Nb-related peaks did not appear, which indicated that the Nb_2O_5 might exist in an amorphous state before heat treatment. The melting point of elemental Sb is approximately 630 °C and the crystallization temperature of niobium oxide is known to be relatively high [32,33]. Therefore, heat treatment was performed at 600 °C. The treatment was carried out for a control sample without the carbon source at the same temperature. In the XRD pattern, peaks for orthorhombic Nb_2O_5 (T-Nb_2O_5, ICDD-JCPDS No. 30-0873) were detected, which revealed that the amorphous phase was transformed into a crystalline structure [29]. The crystallized orthorhombic Nb_2O_5 phase has been known to have advantages for fast Li^+ ion storage [25–28]. Naphthalene was selected as the carbon source for incorporation during heat treatment as reported previously [37]. The XRD pattern after the naphthalene heat treatment was similar to that obtained without the carbon precursor. This indicates that the Sb-Nb_2O_5 composite was successfully prepared.

Carbon incorporation was confirmed from Raman analysis. Figure S1 shows the Raman spectrum of the synthesized material. The spectrum exhibited two bands at around 1350 and 1600 cm^{-1}, which are attributable to the D and G bands of the amorphous carbon layer on the surface of the composite. Several Sb- and Nb-related bands were also observed. TGA was used to measure the carbon content. The composite samples prepared with and without the carbon precursor were heated in air; their weight changes are shown in Figure S2. From approximately 400 °C, both composite materials gained weight, which could be ascribed to Sb oxidation [38]. The carbon-coated sample showed a lower weight gain of 3.7%.

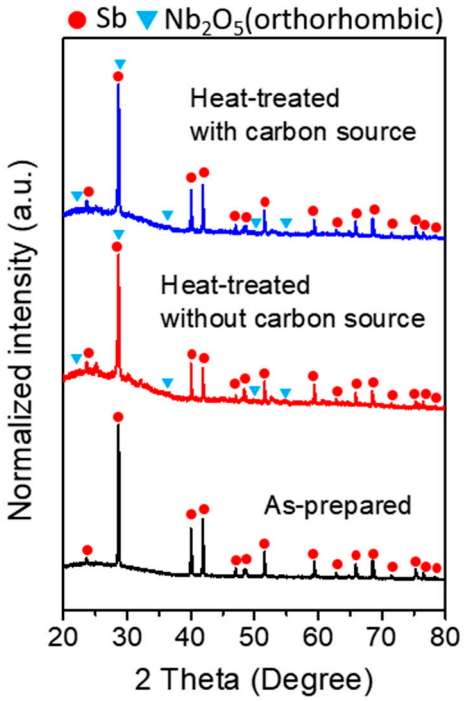

Figure 2. XRD patterns of as-prepared and composite after heat treatment with and without a carbon source.

XPS was adopted to investigate the chemical state of Sb, O, and Nb elements in the composite. Before the measurements, the sample surface was cleaned with argon-ion sputtering for 300 s to remove contaminants. Figure 3 shows the Sb 3d, O 1s, and Nb 3d core-level XPS spectra of the synthesized composite, which were deconvoluted into sub-profiles. Since the Sb 3d and O 1s core-level spectra overlap, the spectra are presented in the same figure (Figure 3a). The profiles obtained from the surface appear to be complex because the composite surface was oxidized with some impurities. After the sputtering, the spectrum attributable to bulk in the composite was demonstrated with further simplified features. The sub-profiles centered at 537.7 and 528.3 eV are attributed to the Sb 3d binding energy of Sb metal (Sb^0) [15–17]. This is related to the core Sb nanoparticles in the composite and corresponds to the Sb diffraction peaks in the XRD pattern. The sub-profiles at 539.7 and 530.4 eV are attributed to Sb^{3+}, which indicates that a small amount of Sb oxide formed in the material. The sub-profile for the binding energy of 530.9 eV could also originate from the O 1s core-level spectra [39], which overlaps the sub-profiles for Sb^{3+} in Sb 3d. The profile could be related to the Nb-O bonds from niobium oxides in the composite [35,39]. The oxidation state of Nb can be analyzed from the Nb 3d core-level spectra (Figure 3b). The sub-profiles at the binding energy of 210.3 and 207.6 eV are assigned to the Nb^{5+} state (Nb_2O_5) [33,35]. The signals for Nb^{5+} can be seen as dominant, which corresponded to the existence of T-Nb_2O_5 in the composite. This feature confirms the XRD analysis result. However, several small sub-profiles attributable to Nb^{4+} and Nb^{2+} also appear, revealing the possible existence of oxygen-deficient oxide forms.

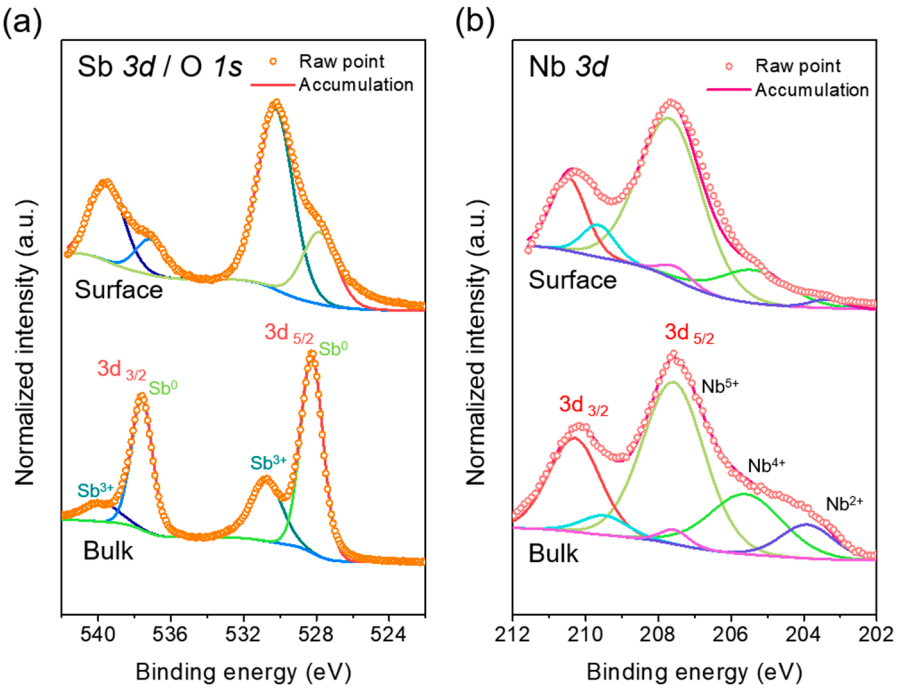

Figure 3. XPS core-level spectra of the composite: (**a**) Sb 3d/O 1s and (**b**) Nb 3d.

Electron microscopy was used to investigate the surface characteristics and morphology of the synthesized composite; the results are shown in Figure 4. Figure 4a,b shows the SEM images of the composite before and after heat treatment at 600 °C. Both images show that the composite has spherical shapes with size ranging from a few hundred nanometers to one micrometer. The spherical composite particles appear to be aggregations of primary nanoparticles. There are no significant morphological changes evident after the heat treatment. Figure 4c exhibits a bright-field TEM image of the synthesized material after the heat-treatment that shows an approximately 150-nanometer core surrounded by other materials to form a core-shell. Figure 4d–f show HR-TEM images of the composite. Two different crystallites were detected in Figure 4d and the marked areas were enlarged into Figure 4e,f (Inset: Fast Fourier Transform (FFT) pattern). In Figure 4e, the d-spacing value (3.11 Å) for the crystallite is assigned to the (012) reflection of Sb metal [40]. In Figure 4f, T-Nb_2O_5 crystallite was identified by the FFT pattern and the d-spacing value of 3.93 Å was attributed to the (001) reflection of T-Nb_2O_5 [27]. The existence of Sb and T-Nb_2O_5 nanocrystallites in the composite was confirmed from these HR-TEM analyses.

To further examine the microstructure of the composite, EDS elemental mapping was performed. Figure 5 presents the TEM image and corresponding EDS elemental mapping images for each element. It can be seen in the TEM image that some core materials were embedded in the composite. In the mapping images, the signals for the Sb element were concentrated on several areas indicating that the Sb metal nanoparticles were the core material. Conversely, Nb and O elements were uniformly distributed over all the composite particles except for the Sb concentration regions. This shows that the surrounding shell material is Nb_2O_5. The C element mapping image demonstrated that carbon was also evenly distributed. This is consistent with the Raman and TGA results that showed the existence of carbon. All the material characterization results, including XRD, XPS, TEM, and EDS, are consistent with a spherical Sb core/Nb_2O_5-C double-shell structured composite.

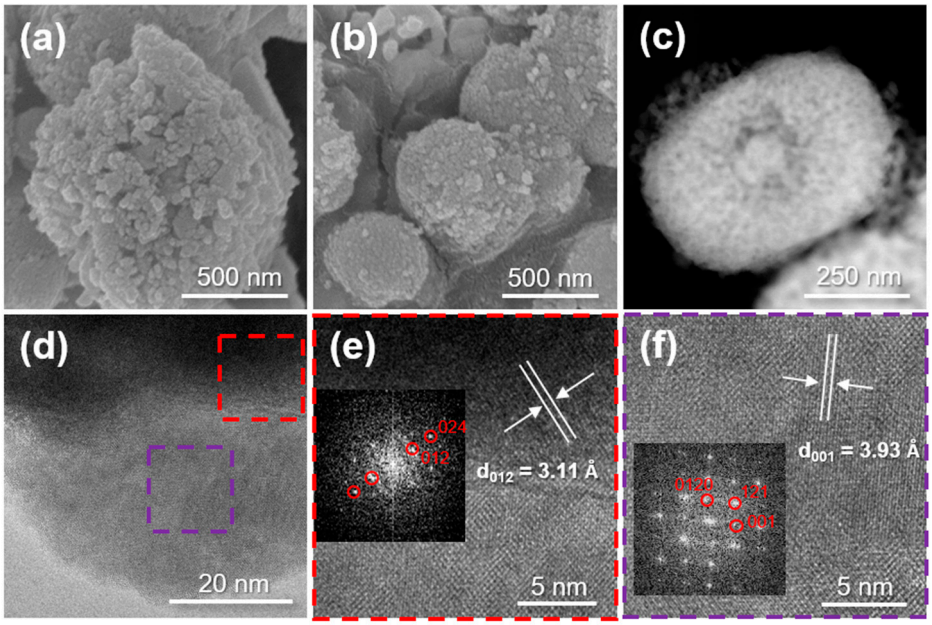

Figure 4. (**a**) FE-SEM image of the composite before heat treatment (as-prepared sample) and (**b**) FE-SEM image, (**c**) bright-field TEM image, and (**d–f**) HR-TEM images of the composite after heat treatment (inset: FFT patterns).

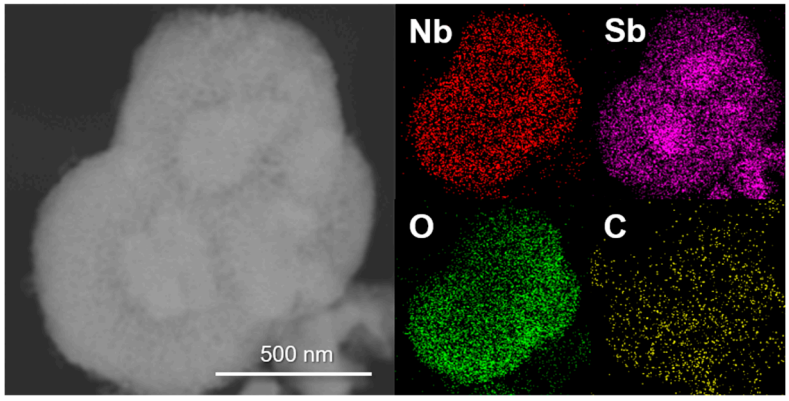

Figure 5. High-magnification TEM image and corresponding EDS elemental mapping results for each element in the spherical Sb core/Nb_2O_5-C double-shell structured composite.

To investigate the composite electrode as an anode for LIBs, electrochemical tests were performed. Figure 6a shows the voltage profiles of the double-shelled composite electrode for the first and second cycles at a rate of 0.15C (100 mA g^{-1}). The discharge and charge capacities of the composite electrode were 833 and 632 mAh g^{-1}, respectively, with an initial coulombic efficiency of 75.9%. To understand the reaction mechanism of the electrode with Li^+, the voltage profiles were converted to differential capacity plots with the results shown in Figure 6b. A broad peak was detected at approximately 1.3 V vs. Li^+/Li during the first discharge process, which is related to the formation of a solid electrolyte interface (SEI) on the surface of the composite. The peak disappeared in the second cycle, indicating that the SEI formation reaction was irreversible. The sharp peak at approximately 0.8 V vs Li^+/Li at discharge is related to the electrochemical alloying reaction from Sb to Li_3Sb phases. During the charging process, the reaction occurred near 1.0 V vs. Li^+/Li, which should be the dealloying reaction of Li_3Sb back to Sb [17]. These electrochemical alloying and dealloying reactions happened during the second cycle, which means that the reactions were reversible. Li insertion and extraction reactions into and from Nb_2O_5 usually occur at a potential range between 1.5 and 2 V vs. Li^+/Li [27,33]. The broad

profiles seen in this potential range during discharge and charge reactions could be related to Nb_2O_5. Similar features are observed in the CV results (Figure S3).

Figure 6c exhibits the cycle performance of the composite electrode measured at a rate of 0.15C (100 mA g^{-1}). For comparison, the cycle performance of pure Sb and mixture (Sb: Nb_2O_5:C = 55:41:4 by wt %, determined based on the estimation of the EDS and TG analysis results) electrodes is given in Figure S4. The Sb core/Nb_2O_5-C double-shelled composite electrode demonstrated much improved cycling stability, compared to the pure Sb and mixture electrodes. This is attributed to the design of the double-shelled structure. The volume changes of the Sb core nanoparticles were reduced by the double shells of Nb_2O_5 and surface carbon coating layer in the composite, so the cycle performance of the electrode was greatly enhanced [5,6]. Figure 6d presents the rate performance of the composite electrode measured at various specific currents from 0.15 to 3C (1C = 660 mA g^{-1}); each step was performed at the same current for both discharge and charge processes. The electrode showed a capacity of approximately 350 mAh g^{-1} at a high current density (3C rate). The rate performance can be credited to the role of the high-rate surrounding T-Nb_2O_5 and the carbon coating layer [33,35]. The T-Nb_2O_5 material is helpful for Li ionic transport and the surface carbon can promote fast electronic and ionic transport through the composite.

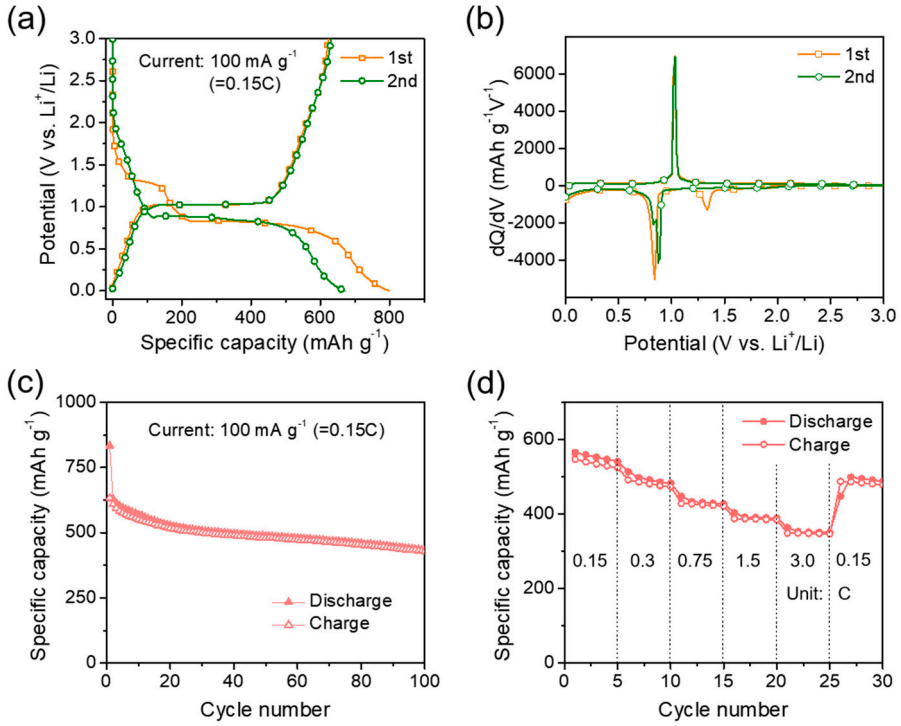

Figure 6. (**a**) Voltage profiles, (**b**) differential capacity plots, (**c**) cycle performance, and (**d**) rate performance of the spherical Sb core/Nb_2O_5-C double-shell structured composite electrode.

4. Conclusions

A spherical Sb core/Nb_2O_5-C double-shell structured composite was synthesized with a simple solvothermal method and subsequent heat-treatment process. Sb metal core nanoparticles were embedded in a Nb_2O_5 composite via the solvothermal precipitation. Then, heat treatment was performed at 600 °C with naphthalene to incorporate carbon and to crystallize amorphous niobium oxide. The microstructure of the synthesized composite was characterized by XRD, XPS, HR-TEM, and EDS analyses, confirming the core/double-shell structure. Electrochemical tests demonstrated that the composite electrode exhibited better cycling stability than pure Sb and mixture electrodes. In the composite, the Nb_2O_5-C double shells buffer the volume change of the Sb nanoparticle cores and help

the cycling stability of the electrode. The shell structure can enhance fast charge transport through the composite particles.

Supplementary Materials: The following are available online at http://www.mdpi.com/1996-1073/13/8/1999/s1, Figure S1: Raman spectrum of the synthesized material, Figure S2: TGA curve of the synthesized material, Figure S3: CV curves of the Sb core/Nb_2O_5-C double-shell structured composite electrode, Figure S4: Cycle performance of the pure Sb and mixture electrodes.

Author Contributions: Conceptualization, H.S., K.K., and J.-H.K.; methodology, H.S.; validation, H.S., K.K., and J.-H.K.; investigation, H.S. and K.K.; data curation, H.S. and J.-H.K.; writing—original draft preparation, H.S.; writing—review and editing, J.-H.K.; supervision, J.-H.K.; project administration, J.-H.K.; funding acquisition, J.-H.K. All authors have read and agreed to the published version of the manuscript.

Funding: This work was supported by the National Research Foundation of Korea (NRF) Grant funded by the Korean Government (2015R1A5A7037615, 2019R1F1A1062835, and 2019R1A6A3A01094741).

Conflicts of Interest: The authors declare no conflict of interest.

References

1. Cheng, X.-B.; Zhang, R.; Zhao, C.-Z.; Zhang, Q. Toward Safe Lithium Metal Anode in Rechargeable Batteries: A Review. *Chem. Rev.* **2017**, *117*, 10403–10473. [CrossRef] [PubMed]
2. Liu, W.; Oh, P.; Liu, X.; Lee, M.-J.; Cho, W.; Chae, S.; Kim, Y.; Cho, J. Nickel-Rich Layered Lithium Transition-Metal Oxide for High-Energy Lithium-Ion Batteries. *Angew. Chem. Int. Ed.* **2015**, *54*, 4440–4457. [CrossRef] [PubMed]
3. Hesse, H.C.; Schimpe, M.; Kucevic, D.; Jossen, A. Lithium-ion battery storage for the grid—A review of stationary battery storage system design tailored for applications in modern power grids. *Energies* **2017**, *10*, 2107. [CrossRef]
4. Winter, M.; Besenhard, J.O.; Spahr, M.E.; Novák, P. Insertion Electrode Materials for Rechargeable Lithium Batteries. *Adv. Mater.* **1998**, *10*, 725–763. [CrossRef]
5. Park, C.-M.; Kim, J.-H.; Kim, H.; Sohn, H.-J. Li-alloy based anode materials for Li secondary batteries. *Chem. Soc. Rev.* **2010**, *39*, 3115–3141. [CrossRef]
6. Obrovac, M.N.; Chevrier, V.L. Alloy Negative Electrodes for Li-Ion Batteries. *Chem. Rev.* **2014**, *114*, 11444–11502. [CrossRef]
7. De Sutter, L.; Berckmans, G.; Marinaro, M.; Smekens, J.; Firouz, Y.; Wohlfahrt-Mehrens, M.; Van Mierlo, J.; Omar, N. Comprehensive aging analysis of volumetric constrained lithium-ion pouch cells with high concentration silicon-alloy anodes. *Energies* **2018**, *11*, 2948. [CrossRef]
8. Li, H.; Zhou, H. Enhancing the performances of Li-ion batteries by carbon-coating: Present and future. *Chem. Commun.* **2012**, *48*, 1201–1217. [CrossRef]
9. He, J.; Wei, Y.; Zhai, T.; Li, H. Antimony-based materials as promising anodes for rechargeable lithium-ion and sodium-ion batteries. *Mater. Chem. Front.* **2018**, *2*, 437–455. [CrossRef]
10. Lv, H.; Qiu, S.; Lu, G.; Fu, Y.; Li, X.; Hu, C.; Liu, J. Nanostructured Antimony/carbon Composite Fibers as Anode Material for Lithium-ion Battery. *Electrochim. Acta* **2015**, *151*, 214–221. [CrossRef]
11. Zhang, X.; Lai, F.; Chen, Z.; He, X.; Li, Q.; Wang, H. Metallic Sb nanoparticles embedded in carbon nanosheets as anode material for lithium ion batteries with superior rate capability and long cycling stability. *Electrochim. Acta* **2018**, *283*, 1689–1694. [CrossRef]
12. Wu, Y.; Pan, Q.; Zheng, F.; Ou, X.; Yang, C.; Xiong, X.; Liu, M.; Hu, D.; Huang, C. Sb@C/expanded graphite as high-performance anode material for lithium ion batteries. *J. Alloys Compd.* **2018**, *744*, 481–486. [CrossRef]
13. Yoon, S.; Manthiram, A. Sb-MO_x-C (M = Al, Ti, or Mo) Nanocomposite Anodes for Lithium-Ion Batteries. *Chem. Mater.* **2009**, *21*, 3898–3904. [CrossRef]
14. Park, C.-M.; Sohn, H.-J. Electrochemical Characteristics of $TiSb_2$ and Sb/TiC/C Nanocomposites as Anodes for Rechargeable Li-Ion Batteries. *J. Electrochem. Soc.* **2010**, *157*, A46–A49. [CrossRef]
15. Sung, J.H.; Park, C.-M. Amorphized Sb-based composite for high-performance Li-ion battery anodes. *J. Electroanal. Chem.* **2013**, *700*, 12–16. [CrossRef]
16. Wang, N.; Bai, Z.; Qian, Y.; Yang, J. One-Dimensional Yolk–Shell Sb@Ti–O–P Nanostructures as a High-Capacity and High-Rate Anode Material for Sodium Ion Batteries. *ACS Appl. Mater. Interfaces* **2017**, *9*, 447–454. [CrossRef]

17. Seo, H.; Kim, H.-S.; Kim, K.; Choi, H.; Kim, J.-H. Magnesium silicide-derived porous Sb-Si-C composite for stable lithium storage. *J. Alloys Compd.* **2019**, *782*, 525–532. [CrossRef]
18. Dailly, A.; Schneider, R.; Billaud, D.; Fort, Y.; Willmann, P. New graphite–antimony composites as anodic materials for lithium-ion batteries.: Preparation, characterisation and electrochemical performance. *Electrochim. Acta* **2002**, *47*, 4207–4212. [CrossRef]
19. Dailly, A.; Ghanbaja, J.; Willmann, P.; Billaud, D. Lithium insertion into new graphite–antimony composites. *Electrochim. Acta* **2003**, *48*, 977–984. [CrossRef]
20. Fuchsbichler, B.; Stangl, C.; Kren, H.; Uhlig, F.; Koller, S. High capacity graphite–silicon composite anode material for lithium-ion batteries. *J. Power Sources* **2011**, *196*, 2889–2892. [CrossRef]
21. Wang, N.; Bai, Z.; Qian, Y.; Yang, J. Double-Walled Sb@TiO_{2-x} Nanotubes as a Superior High-Rate and Ultralong-Lifespan Anode Material for Na-Ion and Li-Ion Batteries. *Adv. Mater.* **2016**, *28*, 4126–4133. [CrossRef] [PubMed]
22. Huang, Y.; Ji, C.; Pan, Q.; Zhang, X.; Zhang, J.; Wang, H.; Liao, T.; Li, Q. Scalable synthesis of Sb/MoS_2/C composite as high performance anode material for lithium ion batteries. *J. Alloys Compd.* **2017**, *728*, 1139–1145. [CrossRef]
23. Choi, H.; Kim, K.; Cho, W.; Park, C.-M.; Kim, J.-H. Synthesis and electrochemical reaction mechanism of Zn-TiO_x-C nanocomposite anode materials for Li secondary batteries. *J. Electrochem. Soc.* **2017**, *164*, A2683–A2688. [CrossRef]
24. Wang, X.; Li, G.; Chen, Z.; Augustyn, V.; Ma, X.; Wang, G.; Dunn, B.; Lu, Y. High-Performance Supercapacitors Based on Nanocomposites of Nb_2O_5 Nanocrystals and Carbon Nanotubes. *Adv. Energy Mater.* **2011**, *1*, 1089–1093. [CrossRef]
25. Augustyn, V.; Come, J.; Lowe, M.A.; Kim, J.W.; Taberna, P.-L.; Tolbert, S.H.; Abruña, H.D.; Simon, P.; Dunn, B. High-rate electrochemical energy storage through Li+ intercalation pseudocapacitance. *Nat. Mater.* **2013**, *12*, 518–522. [CrossRef]
26. Kong, L.; Zhang, C.; Wang, J.; Qiao, W.; Ling, L.; Long, D. Free-Standing T-Nb_2O_5/Graphene Composite Papers with Ultrahigh Gravimetric/Volumetric Capacitance for Li-Ion Intercalation Pseudocapacitor. *ACS Nano* **2015**, *9*, 11200–11208. [CrossRef]
27. Lim, E.; Jo, C.; Kim, H.; Kim, M.-H.; Mun, Y.; Chun, J.; Ye, Y.; Hwang, J.; Ha, K.-S.; Roh, K.C.; et al. Facile Synthesis of Nb_2O_5@Carbon Core–Shell Nanocrystals with Controlled Crystalline Structure for High-Power Anodes in Hybrid Supercapacitors. *ACS Nano* **2015**, *9*, 7497–7505. [CrossRef]
28. Come, J.; Augustyn, V.; Kim, J.W.; Rozier, P.; Taberna, P.-L.; Gogotsi, P.; Long, J.W.; Dunn, B.; Simon, P. Electrochemical Kinetics of Nanostructured Nb_2O_5 Electrodes. *J. Electrochem. Soc.* **2014**, *161*, A718–A725. [CrossRef]
29. Kim, K.; Kim, M.-S.; Cha, P.-R.; Kang, S.H.; Kim, J.-H. Structural Modification of Self-Organized Nanoporous Niobium Oxide via Hydrogen Treatment. *Chem. Mater.* **2016**, *28*, 1453–1461. [CrossRef]
30. Viet, A.L.; Reddy, M.V.; Jose, R.; Chowdari, B.V.R.; Ramakrishna, S. Nanostructured Nb_2O_5 Polymorphs by Electrospinning for Rechargeable Lithium Batteries. *J. Phys. Chem. C* **2010**, *114*, 664–671. [CrossRef]
31. Rani, R.A.; Zoolfakar, A.S.; O'Mullane, A.P.; Austin, M.W.; Kalantar-Zadeh, K. Thin films and nanostructures of niobium pentoxide: Fundamental properties, synthesis methods and applications. *J. Mater. Chem. A* **2014**, *2*, 15683–15703. [CrossRef]
32. Kong, L.; Cao, X.; Wang, J.; Qiao, W.; Ling, L.; Long, D. Revisiting Li^+ intercalation into various crystalline phases of Nb_2O_5 anchored on graphene sheets as pseudocapacitive electrodes. *J. Power Sources* **2016**, *309*, 42–49. [CrossRef]
33. Kim, K.; Woo, S.-G.; Jo, Y.N.; Lee, J.; Kim, J.-H. Niobium oxide nanoparticle core–amorphous carbon shell structure for fast reversible lithium storage. *Electrochim. Acta* **2017**, *240*, 316–322. [CrossRef]
34. Wang, G.; Wen, Z.; Du, L.; Li, S.; Ji, S.; Sun, J. A core–shell Si@Nb_2O_5 composite as an anode material for lithium-ion batteries. *RSC Adv.* **2016**, *6*, 39728–39733. [CrossRef]
35. Kim, K.; Kim, J.-H. Bottom-up self-assembly of nano-netting cluster microspheres as high-performance lithium storage materials. *J. Mater. Chem. A* **2018**, *6*, 13321–13330. [CrossRef]
36. Kim, K.; Seo, H.; Kim, H.-S.; Lee, H.S.; Kim, J.-H. Three-dimensional Ge/GeO_2 shell-encapsulated Nb_2O_5 nanoparticle assemblies for high-performance lithium-ion battery anodes. *Electrochim. Acta* **2020**, *340*, 135952. [CrossRef]

37. Yu, B.-C.; Hwa, Y.; Kim, J.-H.; Sohn, H.-J. Carbon coating for Si nanomaterials as high-capacity lithium battery electrodes. *Electrochem. Commun.* **2014**, *46*, 144–147. [CrossRef]
38. Li, P.; Yu, L.; Ji, S.; Xu, X.; Liu, Z.; Liu, J.; Liu, J. Facile synthesis of three-dimensional porous interconnected carbon matrix embedded with Sb nanoparticles as superior anode for Na-ion batteries. *Chem. Eng. J.* **2019**, *374*, 502–510. [CrossRef]
39. Atuchin, V.V.; Kalabin, I.E.; Kesler, V.G.; Pervukhina, N.V. Nb 3d and O 1s core levels and chemical bonding in niobates. *J. Electron Spectrosc.* **2005**, *142*, 129–134. [CrossRef]
40. Zhang, N.; Liu, Y.; Lu, Y.; Han, X.; Cheng, F.; Chen, J. Spherical nano-Sb@C composite as a high-rate and ultra-stable anode material for sodium-ion batteries. *Nano Res.* **2015**, *8*, 3384–3393. [CrossRef]